Defect-enhanced polarization switching in the improper ferroelectric $LuFeO_3$

P. Barrozo[1,2,3], D. R. Småbråten[4], Y.L. Tang[2,3], P. Bhagwati[1,2,3], S. Saremeini[2], V. Thakare[2], R. Steinhardt[5], M. Holtz[5], V. A. Stoica[6], L. W. Martin[2,3], D. G. Schlom[5], S. M. Selbach[4], R. Ramesh[2,3]

[1] Physics Department, Federal University of Sergipe, São Cristóvão, Sergipe 49100-000, Brazil

[2] Department of Materials Science and Engineering, and Department of Physics, University of California, Berkeley, California 94720, USA

[3] Materials Sciences Division, Lawrence Berkeley National Laboratory, Berkeley CA 94720, USA

[4] Department of Materials Science and Engineering, NTNU Norwegian University of Science and Technology, Norway.

[5] Department of Materials Science and Engineering, Cornell University, Ithaca, NY 15805

[6] Department of Materials Science and Engineering, Pennsylvania State University, University Park, Pennsylvania 16802, USA

Corresponding author: Petrucio Barrozo (e-mail: petruciobarrozo@ufs.br), R. Ramesh (e-mail: ramesh@berkeley.edu)

We present results of switching behavior of the improper ferroelectric $LuFeO_3$. Using a model set of films prepared under controlled chemical and growth-rate conditions, it is shown that defects can reduce the quasi-static switching voltage by up to 40% in qualitative agreement with first-principles calculations. Switching studies show that the coercive field has a stronger frequency dispersion for the improper ferroelectrics compared to a proper ferroelectric such as $PbTiO_3$. We conclude that the primary structural order parameter controls the switching dynamics of such improper ferroelectrics.

Keywords: $LuFeO_3$, h-LFO, ferroelectricity, multiferroic

Introduction

Prototypical "proper" ferroelectrics such as $BaTiO_3$ (BTO), $PbZr_{1-x}Ti_xO_3$ (PZT), and $PbTiO_3$ (PTO) have been intensively studied for several decades for applications such as piezoelectric devices and non-volatile random-access memories (FE-RAMs)[1,2,3]. In such proper ferroelectrics, the spontaneous polarization is the primary order parameter emerging from the transition to a ferroelectric state at the Curie temperature T_C. Many of the applications for such materials rely on there being sufficient field-driven evolution of polarization and mobility of the ferroelectric domain walls to enable polarization switching. Defects, such as oxygen vacancies, are generally considered to be detrimental to ferroelectric properties and are often key causes for reduced switchable polarization (via the pinning of domain walls), fatigue, imprint, pinched ferroelectric hysteresis loops[4].

The polar order in improper ferroelectrics, on the other hand, is a secondary effect coupled to a primary-order parameter that is often a structural distortion. In the improper ferroelectric hexagonal manganite h-RMnO$_3$ (R = Sc, Y, In, Ho, Lu) the polarization has a tri-linear coupling to the primary structural-order parameter. The improper ferroelectric hexagonal $LuFeO_3$ (h-LFO) is iso-structural with h-RMnO$_3$ and is also an improper ferroelectric with a $T_C \approx 1020$ K and antiferromagnetic Neel temperature $T_N \approx 150$ K[5,6]. While polarization switching has been extensively studied for proper ferroelectric perovskites[7,8,9,10,11], little is known about switching in the improper ferroelectrics, let alone the role of point defects on the domain-wall dynamics and switching processes. In general, switching dynamics can be probed either in the time[12] or frequency domain (*e.g.*, by probing the frequency-dependence of the coercive field or voltage) as a function of the ferroelectric layer thickness thus providing details about the domain nucleation and growth process[13,14]. The thickness (t) dependence of the coercive field has been classically described by interface nucleation and growth processes, first described by Kay and Dunn[15] in a model that predicts a $t^{-2/3}$ dependence of the coercive field. Numerous studies on thin films of proper ferroelectrics have validated, at least empirically, this model over thicknesses ranging from a few nanometers to several millimeters[16,17,18,19,20,21].

Thus, while the switching dynamics of proper ferroelectrics is generally well established, a corresponding understanding of improper ferroelectrics such as h-LFO is missing, possibly because there are not as many exemplars of improper ferroelectrics. Since the polar order is a consequence of the primary structural distortion, one would intuitively expect a strong convolution of structural effects in the switching process. Given the lack of a detailed understanding of the polarization dynamics in such improper ferroelectrics, we have initiated a comprehensive study of the same. Here, we study this switching process in epitaxial thin films of h-LFO, with particular attention to the influence of the oxygen (non-)stoichiometry through a combination of *ab initio* calculations and controlled synthesis coupled with detailed frequency-dependent studies of the switching field.

The unit cell of the hexagonal ferrites (*h*-$RFeO_3$) has four layers: two FeO layers and two LuO_2 layers where the lutetium cations are displaced along the *c* axis in a two-up/one-down corrugated pattern (Figure 1a). In the Fe-O layers, the iron cations are surrounded by five oxygens (three in the same plane as the iron and one above and below that layer), forming FeO_5 trigonal bipyramids[22]. The FeO_5 polyhedra share corners in the *a*-*b* plane and are separated by layers of lutetium (Figure1a-b). The structural shift of the lutetium-layer relative to the Fe-O layers breaks inversion symmetry and is responsible for the improper ferroelectricity, resulting in a saturation polarization of ~6 $\mu C/cm^2$ at room temperature[23]. The Lu-O_2 and Fe-O layers are linked through the out-of-plane Lu-O bonds along the polar axis, while the lutetium cations are surrounded by eight oxygen ions (six in the same plane as the Lu-O_2 layers and one above and below that layer) forming LuO_8 polyhedra. The FeO_5 trigonal bipyramids are also rotated about the [120], which is responsible for the broken inversion symmetry of the *h*-$LuFeO_3$ structure, allowing for the emergence of ferroelectric order[24]. Similar to $YMnO_3$[25,26,27], h-LFO is expected to be able to accommodate large oxygen nonstoichiometry.

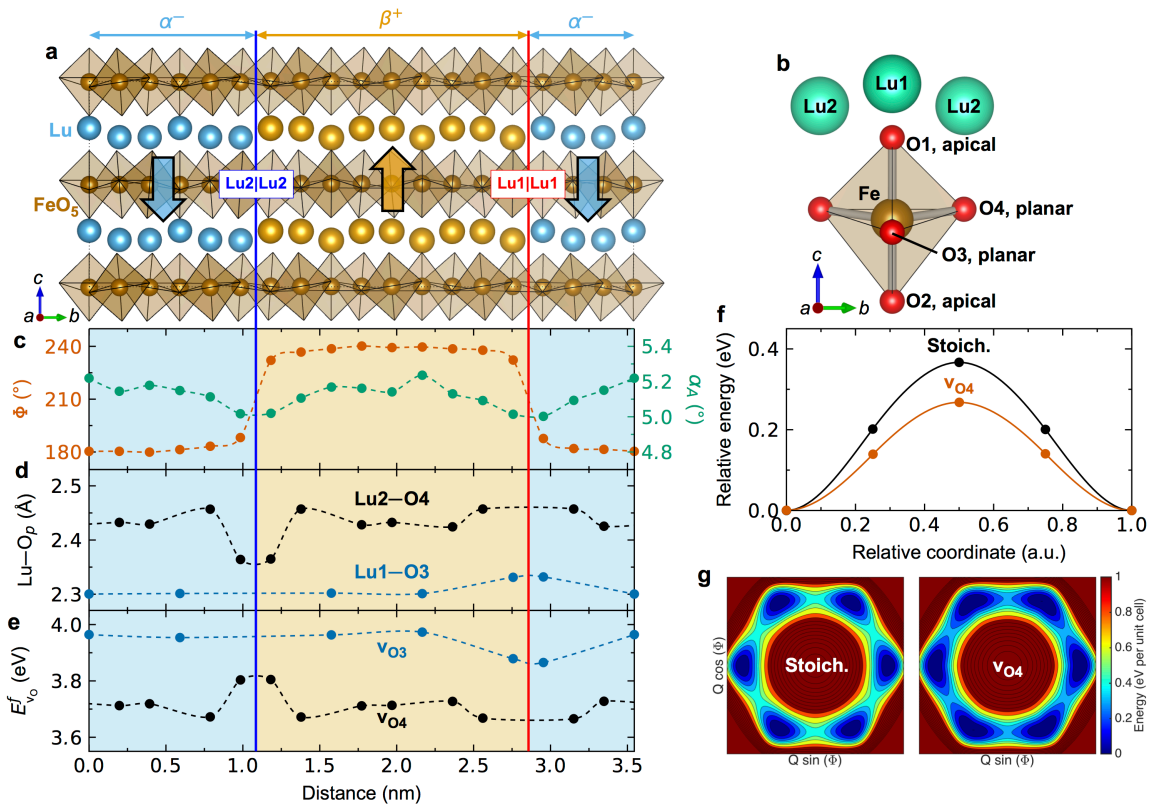

Figure 1 | Interaction of neutral ferroelectric domain walls with oxygen vacancies. (a) Supercell for DFT calculations including two neutral domain walls (blue and red are terminated by Lu2 and Lu1, respectively). (b) Illustration of FeO_5 trigonal bipyramid and symmetry-inequivalent O and Lu positions. (c) Calculated order parameter amplitude Q and phase ϕ across the stoichiometric supercell in (a). Q is here represented by the FeO_5 trigonal bipyramid tilt angle α_A with respect to the ab-plane, while the azimuthal phase ϕ refers to the angle of the trimerization distortion. Dashed lines are guides to the eye. (d) Calculated Lu–O_p bond lengths across the supercell, illustrating the local strain fields near the two walls. (e) Formation energies of vacancies of type O3 and O4, as illustrated in (b) at different positions across the supercell shown in (a). The Lu1 and Lu2 terminated walls are not equivalent because of different coordination environments at these walls (see Supplementary Material). Dashed lines are guides to the eye. (f) Calculated domain wall migration energy barriers for Lu2 terminated wall in the absence and presence of an O4 oxygen vacancy. (g) Approximated "Mexican-hat" free energy landscape for $LuFeO_3$ with and without an O4 oxygen vacancy. Dashed lines in (c)-(e) are guides to the eye.

First-principles calculations (Methods) show that, as in $YMnO_3$, planar oxygen vacancies (O3 and O4, Figure 1b) are strongly favored over apical (O1 and O2)[28] (Supplemental Info.). To investigate the interplay between oxygen vacancies and ferroelectric domain walls in h-LFO, DFT calculations were performed on supercells with two neutral domain walls, one Lu1 and one Lu2 terminated (Figure 1a). The evolution of the crystal structure across the domain wall, represented by the order-parameter phase ϕ and amplitude Q, quantified by the FeO_5 planar tilt angle Φ and the apical tilt angle α_P relative to the [001], respectively (Figure 1c), is similar to that of isostructural $YMnO_3$ [29].

At neutral domain walls there is no internal electric field that can drive accumulation or depletion of oxygen vacancies; only elastic strain fields arising from the discontinuity in the structural order parameter across the walls can drive defect accumulation or segregation. To visualize the local nature of such elastic strain fields the bond lengths between the lutetium cations and planar oxygen are shown (Figure 1d), from which it is also evident that the local environments at Lu1- and Lu2-terminated walls differ (Supplemental Info.); a feature that is also found for domain walls in h-$R$$MnO_3$ systems[30]. In contrast with proper ferroelectrics, the calculations show that oxygen vacancies should not accumulate at the domain walls. While the energy of oxygen vacancy in site O3 (see Figure 1d-e) (v_{O3}) are found to be more stable at Lu1-terminated walls, the oxygen vacancy in site O4 (v_{O4}) are more stable v_{O4} in the bulk of a domain than at the Lu2-terminated walls. As v_{O4} are 0.25 eV lower in energy than v_{O3}, the oxygen vacancies are expected to have sufficient mobility to reach their most stable positions during post-synthesis cooling. Only v_{O4} is considered in the following analysis.

To address the impact of oxygen vacancies on the macroscopic ferroelectric response, climbing-image nudged elastic band (Ci-NEB) calculations were done to quantify the domain-wall-migration energy barrier in the presence and absence of oxygen vacancies. We find that an oxygen vacancy reduces the domain-wall-migration energy barrier by ~27% from 0.37 eV in stoichiometric materials to 0.27 eV in the presence of a v_{O4} vacancy (Figure 1f). Macroscopically, this implies that the coercive field should be smaller in oxygen-deficient h-LFO than in stoichiometric versions, as the energy barrier

for switching the polarization is reduced, as illustrated by the flattened energy landscape in the brim of the approximated Mexican-hat potential (Figure 1g).

With this theoretical framework as the background, we next focus on experimental results which show that the oxygen-defect chemistry (and thus the switching characteristics) of the h-LFO thin film can be systematically controlled during growth: 1) by annealing in different oxygen pressures and 2) by varying the frequency of the laser pulses and thus the deposition rate (details of the deposition process are presented, Supplemental Info.). We used an epitaxial top and bottom layer of tin-doped indium oxide (ITO) that promotes (001)-oriented epitaxial growth of the h-LFO, as evidenced by the lack of any other crystallographic orientations from X-ray diffraction studies (Figure 2a) as well as reciprocal space maps (RSMs, Figures 2c, d). The reduction of intensity in the 002 peak of h-LFO grown in different conditions (Figure 2a) can be attributed to the creation of oxygen vacancies related by the changing the oxygen pressure during cooling or the laser repetition rate at growth. The shift of the 002-diffraction peak towards lower Bragg angles with less oxidizing conditions and higher deposition frequency indicates an increase of the out-of-plane lattice parameter, similar to that reported for the $YMnO_3$ [31]. The full-width-at-half-maximum (FWHM) of films grown under different conditions (growth pressures and laser repetition rates) indicate that the crystallinity of the h-LFO films can be tuned by changing the oxygen annealing pressure or by controlling the deposition rate during the growth (Figure 2b). RSM's for the h-LFO heterostructures grown with optimal conditions by PLD reveal good epitaxy for the 60-nm-thick films annealed at 750 Torr (Figure 2c) and 20 mTorr (Figure 2d) of oxygen.

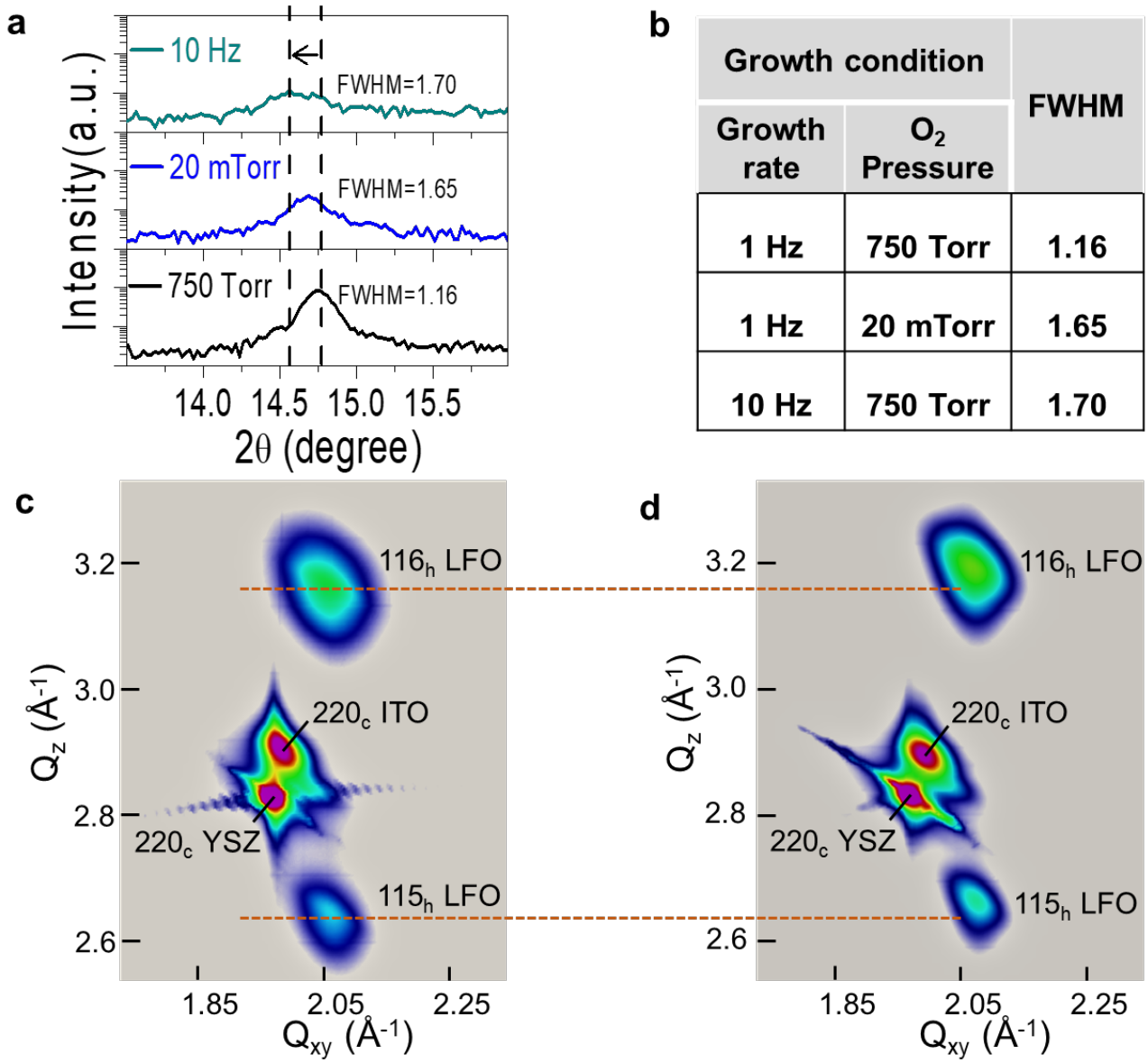

Growth condition		FWHM
Growth rate	O_2 Pressure	
1 Hz	750 Torr	1.16
1 Hz	20 mTorr	1.65
10 Hz	750 Torr	1.70

Figure 2: (a) X-ray diffraction of the (002) peak of 60 nm thick h-LFO thin film produced by PLD and grown at 10 Hz (cooled in 750 Torr of O_2), grown at 1 Hz and cooled in 750 Torr O_2 and cooled in 20 mTorr of O_2. (b) Table to show the FWHM of films grown under different conditions; (c), (d) are reciprocal space maps of samples cooled at 750 Torr and 20 mTorr, respectively.

HR-STEM studies provide a direct, microscopic picture of defects and local structural changes. The optimally cooled (750 Torr of oxygen) heterostructures show a highly ordered structure; the trimerization structure of two-up/one-down cations can also be observed (zoom-in, Figure 3a). The samples cooled in 20 mTorr of oxygen (Figure 3b) and the sample grown at faster deposition rates 10 Hz both show a higher density of stacking defects if compared with optimal growth condition showed in Figure 3a. At higher resolution, these defects are resolved to be a mixture of stacking defects can be illustrated in the HR-STEM images (Supplementary Figure S3- a and b). The disturbed region where a continuous increase of the vertical coordinates like a 1-2-3 staircase is illustrated in the Supplementary Figure S3-c. We can observe that the 1-2-3 staircase can be associated with the region between different polarization and then can be attributed to the domain wall region.

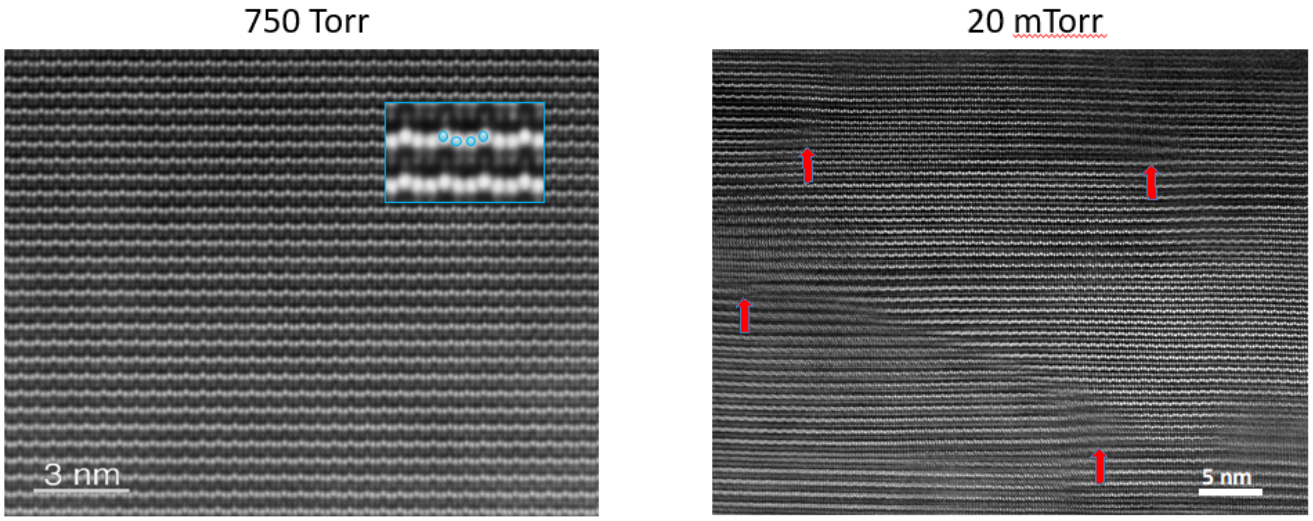

Figure 3: (a) HRSTEM of defect-free structure in 750 Torr sample; (b) HRSTEM of defects in 20 mTorr sample.

We now turn to detailed ferroelectric measurements. In order to explore (and reduce) the influence of leakage, the measurements were carried out at both 100 K and 300 K (ferroelectric hysteresis loops completed at 300 K are shown in Supplementary Figure S4). The leakage current at

100 K (Supplementary Figure S5) is small enough to allow us to investigate the polarization switching behavior across a wide frequency range (*i.e.*, from 50 mHz to 100 kHz – nearly 6 orders of magnitude). The ferroelectric hysteresis loops for four representative h-LFO samples, at a fixed frequency of 25 kHz, are provided for comparison (Figs. 4a-d). The corresponding frequency dependence is also provided in Supplementary Fig. S6. The first key observation is that all samples show well-saturated hysteresis loops at 100 K. An interesting feature is that the coercive field is progressively reduced by the introduction of defects during growth, both by depositing an order of magnitude faster (PLD growth at 10 Hz vs. 1 Hz; Fig. 4a and b, respectively) or by cooling the film in a less oxidizing environment (PLD growth at 1 Hz and cooled in 20 mTorr vs. 750 Torr; Fig. 4a and c, respectively). This reduction of coercive field with increase in defect concentration is consistent with our theoretical finding that oxygen vacancies reduce the domain-wall-migration barrier.

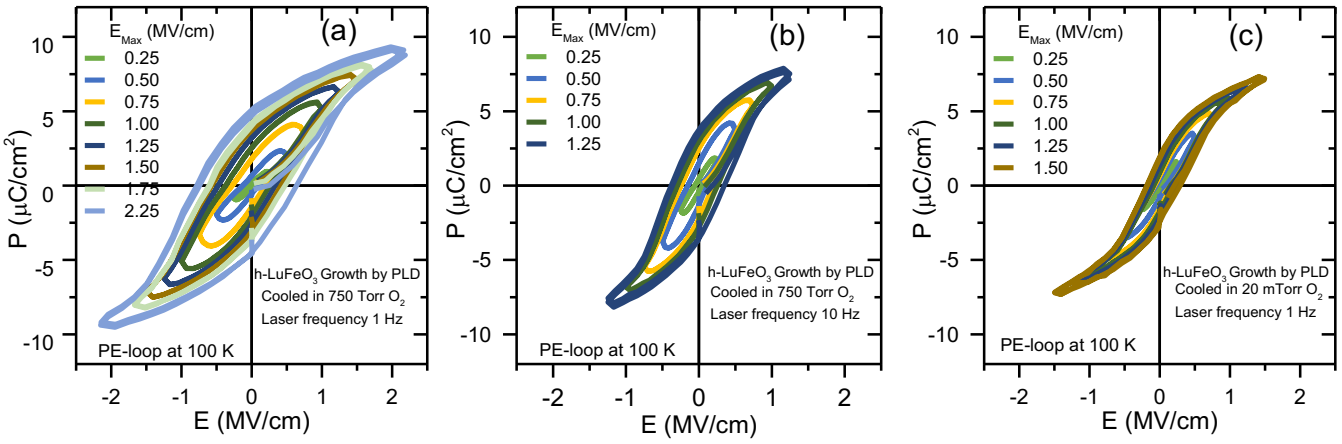

Figure 4: Ferroelectric hysteresis loops of the four Pt/ITO/LFO/ITO model systems used in this study at 100 K. (a) grown at a deposition rate of 1 Hz, cooled in 750 Torr of oxygen; (b) grown at 10 Hz and cooled in 750 Torr of oxygen; (c) grown at 1 Hz and cooled in 20 mTorr of oxygen.

Next we explored the role of the changing growth conditions on the frequency dependence of the coercive field. For classical ferroelectrics, the Ishibashi & Orihara model[32] describes the dynamics of the domain walls under the influence of either an AC or pulsed external field. The domain-wall

velocity is a function of only the applied field E (*i.e.*, v(E,t)) and the volume of the domain switching at a time t is described as a power law of the growth dimension, d. In this model, the coercive field is described by: $E_c = E_{c,0} + a\, f^{\,b}$, where f is the measurement frequency, $E_{c,0}$ is the limiting value of the switching field (*i.e.*, the quasi-static field at zero frequency $E_{c,0}$), and a and b are obtained from fits to the frequency dependent data. The frequency dependence of the coercive field is captured through the exponent "b". To eliminate the effects of small shifts of the hysteresis loops (for example, due to internal fields), we have plotted the average coercive field ($[E_c^+ - (-E_c^-) = 2E_c]/2$) versus frequency. The frequency dependence of this average coercive field was extracted from the ferroelectric hysteresis loops for at least 20 capacitors on each sample and for multiple samples for each growth condition. We plot the coercive field as a function of log(f) for all samples (Figure 5). For comparison, we include data for $PbTiO_3$ as a representative proper ferroelectric. The data were fitted using the Ishibashi model (solid lines, Figure 5). The data for each of the samples fits well to this model (with regression coefficients in the 0.93-0.99 range), albeit with significantly different exponents, which we explain next.

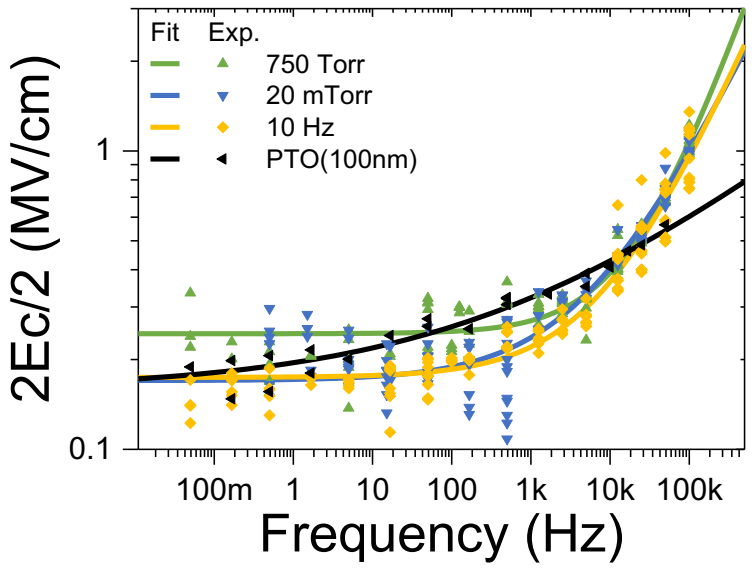

Figure 5: Coercive field as a function of frequency for LFO samples grown at different conditions and for PTO. The solid lines are fits to the experimental data using a power law described by the Ishibashi model

There are several key observations from this frequency-dependent data (summarized in Table I). First, as expected, all of the samples show a frequency dependence of the coercive field – that of the proper ferroelectric ($PbTiO_3$) can be fitted well to a power law behavior with an exponent of b ≈ 1/4; this is consistent with previous reports[33,34]. Second, as we already observed in the ferroelectric hysteresis loops (Figure 4), the defective h-LFO samples show a lower E_c^0 (by ~40%) as compared to PLD samples cooled in 750 Torr of oxygen. Most importantly, however, the value of the exponent *b* for all of the h-LFO samples is ~0.66. To get a more unified picture, we have normalized the average coercive field by plotting $[E_c\text{-}E_c^0/a]$ as a function of frequency (Supplementary Figure S7). The proper ferroelectric ($PbTiO_3$) maps onto each other with a slope of ~1/4. In contrast, the improper ferroelectric samples in this paper that have a large slope that is approximately the same ~2/3 for all sample studied here. Thus, from the data (Figure 5 and S7), we observe a clear difference in switching dynamics between the improper (h-LFO) and proper (PTO) ferroelectrics. This difference can be attributed to the thickness reduction. All improper ferroelectric studied have 60 nm for this the b parameter is around the same for all sample, this results suggest that each material have a dependence with the thickness where in large thickness the b parameter is like 1/4 but this value is increase with the thickness reduction. The ratio with the increase of the b parameter depend of the material and this study will be very important to understand the dynamics of ferroelectrics.

We explain the difference in the exponent *b* in terms of the details of the switching process using the Ishibashi model[32] where the frequency dependence of the coercive field follows a simple power law $E_c \propto f^b$. From symmetry considerations, the h-LFO must display the same topologically protected domain structure as the more studied hexagonal manganites[35,36]. In this topologically protected vortex-antivortex pattern, the stripe-like domain cannot simply disappear. In this case, two

boundary domain walls of the stripe-like domains can merge into an unstable broad wall, that splits again into the two domain walls when the external applied field is reduced[37].Instead of nucleation and growth, polarization switching is therefore expected to occur through domain-wall movement yielding growth of domains with polarization parallel to the applied field, and opposite for domains with antiparallel polarization[38,39].

Another possible scenario involves the structural distortion that is the primary order parameter in such improper ferroelectrics. For a proper ferroelectric, all energy from the external applied field is used to move the DWs and change the polarization. In contrast, for an improper ferroelectric a large portion of the energy is spent on overcoming the structural distortion in the crystal, i.e., move the atoms to rotate the polyhedra, and the balance is available to change the polarization direction.

A fundamental difference between proper ferroelectric perovskites such as $PbTiO_3$ and the improper ferroelectric h-LFO is the interaction between oxygen vacancies and domain walls. While it is well established, both from experiments[40,41] and recent DFT studies[42,43,44,45,46,47,48,49] , that oxygen vacancies segregate to and pin ferroelectric domain walls, this is not the case for improper ferroelectrics like h-LFO and $YMnO_3$[28,29]. Following the extension of the coupling diagram for primary ferroic orders[50] to also include electrochemistry and stoichiometry[51], our results demonstrate a strong and *positive* coupling between ferroelectricity and the chemical potential as a conjugate field. For defects that also give rise to enhanced conductivity, there may be an optimal concentration of defects which reduced the coercive field without causing significant leakage current. Our finding that the presence of an oxygen vacancy reduces the domain-wall-migration barrier opens the possibility of tuning the coercive field through oxygen-vacancy concentration by growth conditions, or even to "reconfigure" a device by post-synthesis annealing. To utilize oxygen stoichiometry to tune the coercive field is particularly promising for improper ferroelectrics where the polarization is less sensitive to point defects[26,28] than conventional perovskites where polarization is the primary order parameter.

In summary, we have examined the coupling between growth condition, crystal defects and polarization switching dynamics in a model "improper" ferroelectric, $LuFeO_3$. There are four key implications from this work. First, the quasi-static switching field can be changed by controlling the defect structure of LFO through growth parameters. Second, in contrast with the proper ferroelectric perovskites $PbTiO_3$, defects reduce the switching field in LFO. This is supported by DFT calculations showing that oxygen vacancies reduce the domain wall migration energy barrier. Third, the frequency dispersion studies of a large number of LFO films as well as PTO films show a universal power dependence of the coercive field on the measurement frequency. Fourth, the exponent of this power dependence is significantly higher for LFO compared to PTO, indicating a key role of the primary structural order parameter on the energetics of the polarization switching.

Table 1: Quasi-static coercive field, $E_{c,0}$, and the frequency dispersion exponent, b, obtained from the fit using the Ishibashi model to describe the mechanism to sweep the polarization for different samples of h-LFO compared with PTO (proper ferroelectrics).

Sample	**$E_{c,0}$(kV/cm)**	**b**
MBE	281	0.61
750 Torr	244	0.77
20 mTorr	170	0.59
10 Hz	174	0.61
PTO	158	0.22

Experimental Section

Sample preparation

ITO/h-LFO/ITO heterostructure growth: epitaxial (20 nm) ITO/(60 nm) h-LFO /(20 nm) ITO were grown on single crystal of 9.5% yttria stabilized zirconia substrate with plane (111) parallel to surface by pulsed-laser deposition (PLD) using a KrF excimer laser ($\lambda = 248$ nm). The 20 nm of ITO used as top and bottom electrode was growing with a laser fluence around 4.5 J/cm^2, partial oxygen pressure of 50 mTorr, 920 K and laser repetition rate of 2 Hz. The 60 nm of hexagonal $LuFeO_3$ (h-LFO) was obtained using a laser fluence of 3.8 J/cm^2, partial oxygen pressure of 20 mTorr, 1090 K and laser repetition rate ranging from 1 Hz to 10 Hz. All three-layer ITO/LFO/ITO was grown in situ, using a base pressure above $1x10^{-6}$ Torr. After deposition of the ITO top-layer the ITO/h-LFO/ITO heterostructure was submitted to an annealing treatment at 1120 K and with different O_2 partial pressure ranging from 20 mTorr to 750 Torr. The density of the structural defects on the h-LFO was induced and controlled by change the laser repetition rate of the LFO layers and by change the partial oxygen pressure on the cooling chamber after the annealing. Capacitor with different diameter sizes were produced by photolithography followed by ion-milling processes. Before the ion milling process a 20nm platinum layer was growth on the structure by sputtering.

Sample characterization

The structural properties were investigated by x-ray diffraction (XRD) and reciprocal space map (RSM) using a Panalytical X'Pert^3 MRD. The microstructure of the Pt/ITO/h-LFO/ITO/YSZ(111) was characterized by high-resolution transmission electron microscopy and Atomic Force Microscopy (show in supplementary materials Figure S2-d). The ferroelectric loops were performed using a Radiant Technologies Precision Multiferroic system attached to a Lake Shore probe station to measurements of electrical properties at temperatures between 100 K to 300 K. Ferroelectric

hysteresis loops were measured at different values of frequency and voltage drive amplitude. We used at least 20 different capacitors to perform the analyses for each frequency and drive amplitude.

Computational details

Density Functional Theory calculations were carried out with VASP using PBEsol and the Lu_3, Fe and and O pseudopotentials. A cutoff of 550 eV was used along with an effective U-J = 3.5 eV applied to Fe 3d. A frustrated ferromagnetic (f-AFM) order on the Fe sublattice was assumed. A Γ-centered $2 \times 2 \times 2$ k-point mesh was used for $(2 \times 2 \times 1)$ supercells with one oxygen vacancy and ions were relaxed until the forces were below 0.005 eV Å^{-1}. The oxygen vacancy formation energy in neutral cells was calculated as $E_{\mathrm{v_O}}^{f} = E_{def} - E_{ref} + \mu_{\mathrm{O}}$ where E_{def} and E_{ref} are the total energies of the oxygen defect cell and the stoichiometric cell, respectively. The chemical potential of oxygen, μ_{O}, was set to μ_{O}= –5 eV, corresponding to typical conditions for PLD.

The structural evolution across domain walls were studied using a $(1 \times 6 \times 1)$ supercell with two parallel domain walls ~18 Å apart and ions were relaxed to forces below 0.01 eV Å^{-1}. Interactions between domain walls and oxygen vacancies were studied using $(2 \times 6 \times 1)$ supercells and ions were relaxed to forces below 0.01 eV Å^{-1}. Segregation enthalpies ΔE_{seg} for the two planar oxygen vacancy sites O3 and O4 were determined by their formation energy profiles across the supercell. Domain wall migration energy barriers were calculated with the Climbing-image Nudged Elastic Band (c-NEB) method. The walls were assumed to migrate as parallel equidistant walls, using 5 intermediate images and with forces on ions relaxed to 0.03 eV Å^{-1}. The free-energy landscape was determined from energy barriers between the domains in using c-NEB as described above, and from the static energy landscape of the $K_3 + \Gamma_2^-$ mode amplitude in $(2 \times 2 \times 1)$ supercells using intermediate structures interpolated between $P6_3/mmc$ and $P6_3cm$ structures with and without oxygen vacancies.

Acknowledgements

Nicola A. Spaldin is acknowledged for helpful discussions. DRS and SMS were supported by the Research Council of Norway (Project no. 231430). The work at Berkeley (P.B.) was supported by the SRC ASCENT project, which is part of the SRC-JUMP program. Computational resources were provided by UNINETT Sigma2 through Projects NN9264K and ntnu243. *Petrucio Barrozo was financed in part by the Coordenação de Aperfeiçoamento de Pessoal de Nível Superior - Brasil (CAPES) - Finance Code 001.*

References

[1] V. Garcia, S. Fusil, K. Bouzehouane, S. Enouz-Vedrenne, N. D. Mathur, A. Barthelemy, M. Bibes, *Nature* **2009**, 460, 81.

[2] M. Okuyama, Y. Hamakawa, *Ferroelectrics* **1985**, 63, 243.

[3] S. Trolier-McKinstry, P. Muralt, *J. Electroceram.* **2004**, 12, 7.

[4] M. E. Lines, A. M. Glass, *Principles and Applications of Ferroelectrics and Related Materials,* Clarendon, Oxford, UK **1977**.

[5] T. Katsufuji, M. Masaki, A. Machida, M. Moritomo, K. Kato, E. Nishibori, M. Takata, M. Sakata, K. Ohoyama, K. Kitazawa, H. Takagi, *Phys. Rev. B* **2002**, 66, 134434.

[6] T. Katsufuji, S. Mori, M. Masaki, Y. Moritomo, N. Yamamoto, H. Takagi, *Phys. Rev. B* **2002**, 64, 104419.

[7] W. Merz, *Phys. Rev.* **1954**, 95, 690.

[8] D. J. Jung, M. Dawber, J. F. Scott, L. J. Sinnamon, J. M. Gregg, *Integr. Ferroelectr.* **2002**, 48, 59.

[9] J. F. Scott, *Integr. Ferroelectr.* **1996**, 12, 71.

[10] P. Chandra, M. Dawber, P. B. Littlewood, J. F. Scott, *Ferroelectrics* **2004**, 313, 7.

[11] P. Gao, C. T. Nelson, J. R. Jokisaari, S.-H. Baek, C. W. Bark, Y. Zhang, E. Wang, D. G. Schlom, C.-B. Eom, X. Pan, *Nat. Commun.* **2011**, 2, 591.

[12]J. Li, B. Nagaraj, H. Liang, W. Cao, Chi. H. Lee, R. Ramesh, *Appl. Phys. Lett.* **2004**, 84, 1174.

[13] Y. Ishibashi, H. Orihara, *Integr. Ferroelectr.* **1995**, 9, 57.

[14] A. K. Tagantsev, L. E. Cross, J. Fousek, *Domains in ferroic crystals and thin films*, Springer-Verlag, New York, US **2010**.

[15] H. F. Kay, J. W. Dunn, *Philos. Mag.* **1962**, 7, 2027.

[16] S. Ren, C. Lu, J. Liu, H. Shen, Y. Wang, *Phys. Rev. B* **1996**, 54, R14337.

[17] J. F. Scott, *J. Phys.: Condens. Matter* **2006**, 18, R361.

[18] M. Dawber, P. Chandra, P. B. Littlewood, J.F. Scott, *J. Phys.: Condens. Matter* **2003**, 15, L393.

[19] J. F. Scott, M. Dawber, A. Q. Jiang, F. D. Morrison, *Ferroelectrics* **2003**, 286, 223.

[20] P. Maksymovych, M. Huijben, M. Pan, S. Jesse, N. Balke, Y. H. Chu, H. J. Chang, A. Y. Borisevich, A. P. Baddorf, G. Rijnders, D. H. A. Blank, R. Ramesh, S. V. Kalinin, *Phys. Rev. B* **2012**, 85, 014119.

[21] O. Trithaveesak, J. Schubert, C. Buchal, *J. Appl. Phys.* **2005**, 98, 114101.

[22] X. Xu, W. Wang, *Mod. Phys. Lett. B* **2014**, 28, 1430008.

[23] Y. K. Jeong, J.-H. Lee, S.-J. Ahn, H. M. Jang, *Chem. Mater.* **2012**, 24, 2426.

[24] H. Das, A. L. Wysocki, Y. Geng, W. Wu, C. J. Fennie, *Nat. Commun* **2014***,* 5, 2998.

[25] C. J. Fennie, K. M. Rabe, *Phys. Rev. B* **2005**, 72, 100103.

[26] S. H. Skjærvø, E. T. Wefring, S. K. Nesdal, N. H. Gaukås, G. H. Olsen, J. Glaum, T. Tybell, S. M. Selbach, *Nat. Commun* **2016**, 7, 13745.

[27] Y. Du, X. Wang, D. Chen, Y. Yu, W. Hao, Z. Cheng, S. X. Dou, *Phys. Chem. Chem. Phys.* **2013**, 15, 20010.

[28] S. H. Skjærvø, D. R. Småbråten, N. A. Spaldin, T. Tybell, S. M. Selbach, *Phys. Rev. B* **2018**, 98, 184102.

[29] J. Schaab, S. H. Skjærvø, S. Krohns, X. Dai, M. E. Holtz, A. Cano, M. Lilienblum, Z. Yan, E. Bourret, D. A. Muller, M. Fiebig, S. M. Selbach, D. Meier, *Nat. Nanotechnol.* **2018**, 13, 1028.

[30] D. R. Småbråten, Q. N. Meier, S. H. Skjærvø, K. Inzani, D. Meier, S. M. Selbach, *Phys. Rev. Mater.* **2018**, 2, 114405.

[31] A. J. Overton, J. L. Best, I. Saratovsky, and M. A. Hayward, *Chem. Mater.* **2009**, 21, 4940.

[32] Y. Ishibashi, H. Orihara, *Integr. Ferroelectr.* **1995**, 9, 57.

[33] H. Orihara, S. Hashimoto, Y. Ishibashi, *J. Phys. Soc. Jpn.* **1964**, 63, 1031.

[34] J. F. Scott, *Integr. Ferroelectr.* **1996**, 12, 71.

[35] S. M. Griffin, M. Lilienblum, K. T. Delaney, Y. Kumagai, M. Fiebig, N. A. Spaldin, *Phys. Rev. X* **2012**, 2, 041022.

[36] S. C. Chae, N. Lee, Y. Horibe, M. Tanimura, S. Mori, B. Gao, S. Carr, S.-W. Cheong, *Phys. Rev. Lett.* **2012**, 108, 167603.

[37] A. Ruff, Z. Li, A. Loidl, J. Schaab, M. Fiebig, A. Cano, Z. Yan, E. Bourret, J. Glaum, D. Meier, S. Krohns, *Appl. Phys. Lett.* **2018**, 112, 182908;

[38] T. Choi, Y. Horibe, H. T. Yi, Y. J. Choi, W. Wu, S.-W. Cheong, *Nat. Mater.* **2010**, 9, 253.

[39] K. L. Yang, Y. Zhang, S. H. Zheng, L. Lin, Z. B. Yan, J.-M. Liu, S.-W. Cheong, *Phys. Rev. B* **2017**, 96, 144103.

[40] S. Aggarwal, R. Ramesh, *Annu. Rev. Mater. Sci.* **1998**, 28, 463.

[41] M. Dawber, J. F. Scott, *Appl. Phys. Lett.* **2000**, 76, 1060.

[42] L. He, D. Vanderbilt, *Phys. Rev. B* **2003**, 68, 134103.

[43] A. Chandrasekaran, X.-K. Wei, L. Feigl, D. Damjanovic, N. Setter, N. Marzari, *Phys. Rev. B* **2016**, 93, 144102.

[44] A. Chandrasekaran, D. Damjanovic, N. Setter, N. Marzari, *Phys. Rev. B* **2013**, 88, 214116.

[45] C. Paillard, G. Geneste, L. Bellaiche, B. Dkhil, *J. Phys.: Condens. Matter* **2019,** 29, 485707.

[46] T. Xu, T. Shimada, Y. Araki, J. Wang, T. Kitamura, *Nano Lett.* **2016**, 16, 454.

[47] X. Y. Li, Q. Yang, J. X. Cao, L. Z. Sun, Q. X. Peng, Y. C. Zhou, R. X. Zhang, *J. Phys. Chem. C* **2018**, 122, 3091.

[48] S. Farokhipoor, C. Magén, S. Venkatesan, J. Íñiguez, C. J. M. Daumont, D. Rubi, E. Snoeck, M. Mostovoy, C. de Graaf, A. Müller, M. Döblinger, C. Scheu, B. Noheda, *Nature* **2014**, 515, 379.

[49] J. J. Gong, C. F. Li, Y. Zhang, Y. Q. Li, S. H. Zheng, K. L. Yang, R. S. Huang, L. Lin, Z. B. Yan, J.-M. Liu, *Materials Today Physics* **2018**, 6, 9.

[50] N. A. Spaldin, M. Fiebig, *Science* **2005**, 309, 391.

[51] S. V. Kalinin, N. A. Spaldin, *Science* **2013**, 341, 858.

Supplementary Section

Defect-enhanced polarization switching in the improper ferroelectric $LuFeO_3$

P. Barrozo[1,2,3], D. R. Småbråten[4], Y.L. Tang[2,3], P. Bhagwati[1,2,3], S. Saremeini[2], V. Thakare[2], R. Steinhardt[5], M. Holtz[5], V. A. Stoica[6], L. W. Martin[2,3], D. G. Schlom[5], S. M. Selbach[4], R. Ramesh[2,3]

[1] Physics Department, Federal University of Sergipe, São Cristóvão, Sergipe 49100-000, Brazil

[2] Department of Materials Science and Engineering, and Department of Physics, University of California, Berkeley, California 94720, USA

[3] Materials Sciences Division, Lawrence Berkeley National Laboratory, Berkeley CA 94720, USA

[4] Department of Materials Science and Engineering, NTNU Norwegian University of Science and Technology, Norway.

[5] Department of Materials Science and Engineering, Cornell University, Ithaca, NY 15805

[6] Department of Materials Science and Engineering, Pennsylvania State University, University Park, Pennsylvania 16802, USA

Corresponding author: Petrucio Barrozo (e-mail: petruciobarrozo@ufs.br), R. Ramesh (e-mail: rramesh@berkeley.edu)

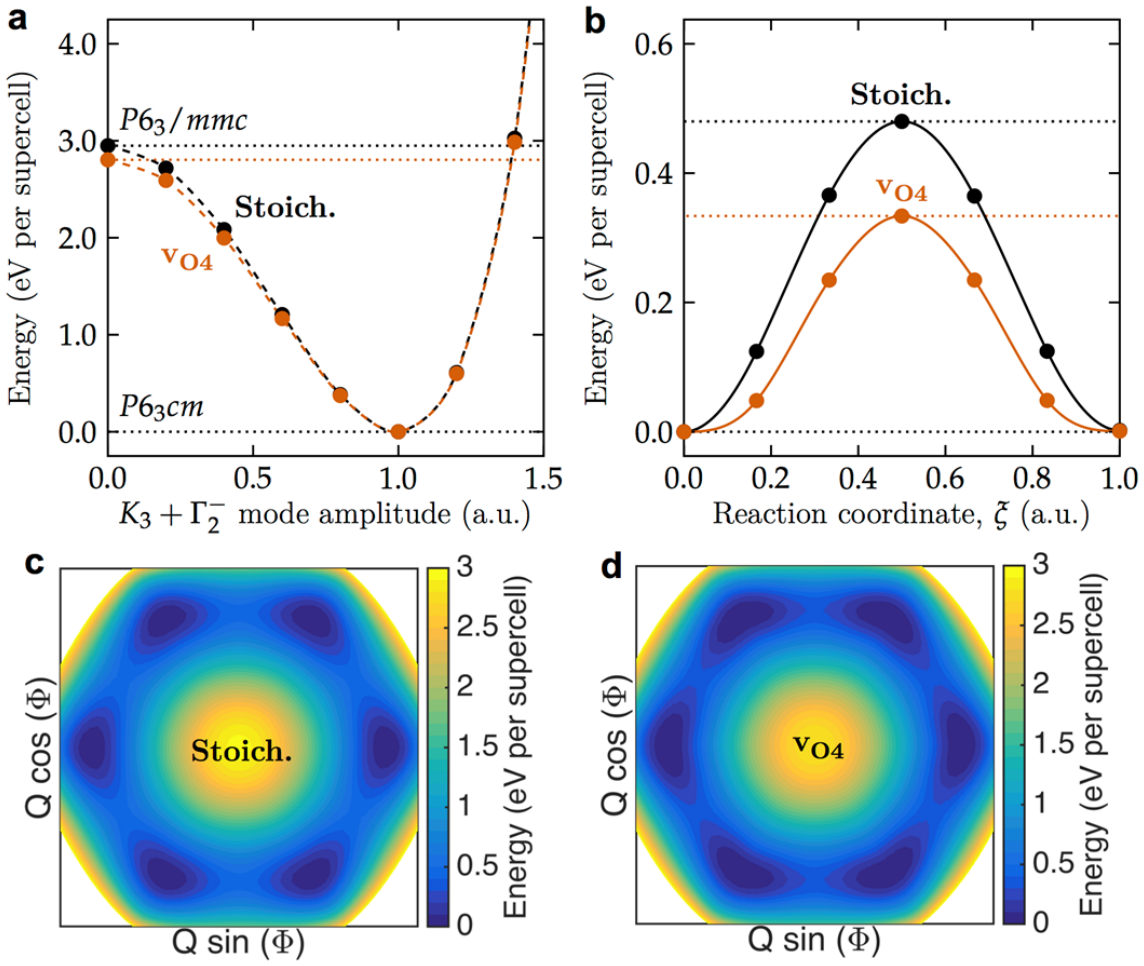

Supplementary Figure S1: **Domain switching and free energy landscape**. Oxygen vacancies affect the domain switching energy and perturb the free energy landscape. Since planar O4 vacancy is energetically most favored, we will in the following focus on this vacancy type only. The static energy landscape for the $K_3 + \Gamma_2^-$ mode amplitude without and with planar O4 vacancy is shown in Figure S1(**a**). The energy difference between the high-symmetry $P6_3/mmc$ phase and the low-symmetry $P6_3cm$ phase is 0.14 eV per supercell for the v_{O4} system. However, no qualitative differences between the two systems in the $K_3 + \Gamma_2^-$ energy landscapes are observed. There is however a significant difference in the domain switching energy barriers (Figure S1(**b**)), where the v_{O4} system has an energy barrier of 0.33 eV per supercell while the stoichiometric system has an

energy barrier of 0.48 eV per supercell. This means that the energy required to switch the electrical polarization is 0.15 eV lower for the system with oxygen vacancies. This is reflected by the interpolated free-energy landscapes for stoichiometric material (Figure S1(**c**)) and for the v_{O4} system (Figure S1(**d**)), which shows a flatter energy surface around the brim of the Mexican hat potential. The reduced domain switching energy can be rationalized from the structural accommodation of the planar O4 vacancy, where v_{O4} gives a change in (Φ, Q) resembling the (hypothetical) $P\bar{3}c1$ symmetry at the saddle point between the domains (*i.e.* the domain wall center).

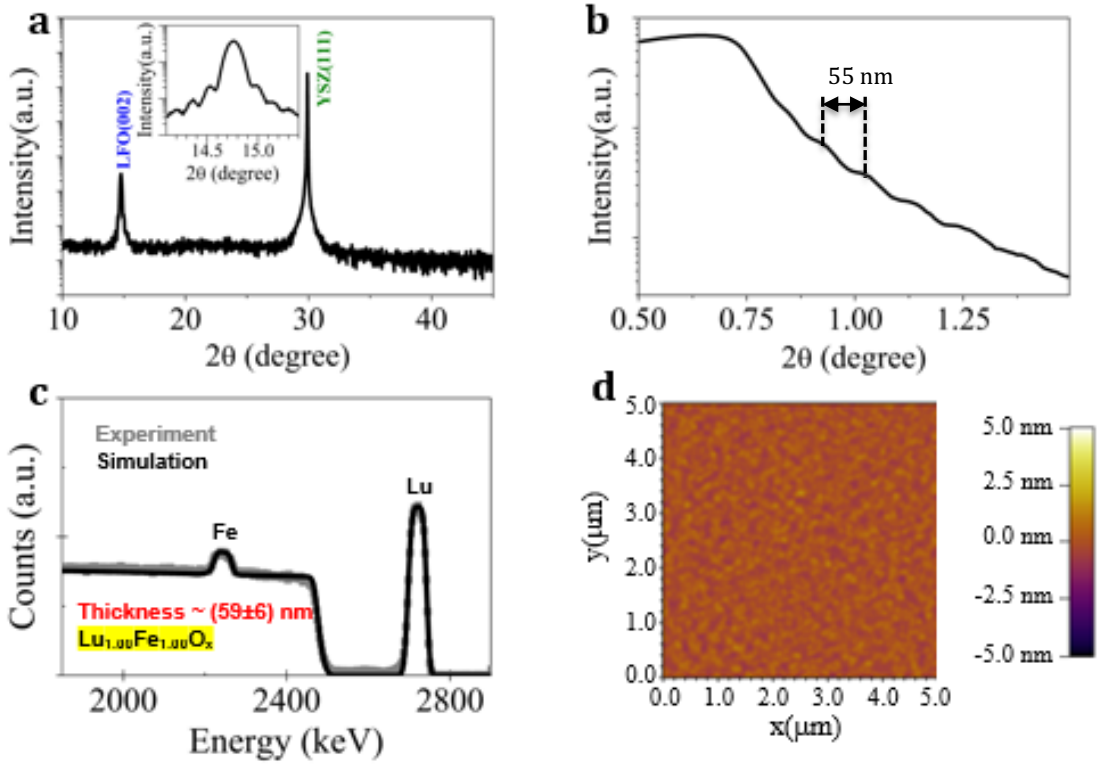

Supplementary Figure S2: **Optimization of the $LuFeO_3$ growth conditions.** In addition to the properties shown in the main text, we have explored a wide range of synthesis conditions to obtain a stoichiometric, single phase of the hexagonal $LuFeO_3$ (h-LFO) phase by pulsed laser deposition. In Figure S2(a) we show the X-rays diffraction patterns (XRD) of h-LFO grown on YSZ (111) substrate using a laser fluence of 2.6 J/cm^2 and an oxygen partial pressure of 20 mTorr. The (004) peak of the h-LFO are superposed on the (111) substrate peak. Figure S2(b): shows the X-ray reflectometry data that yields a thickness of ~55 nm. Figure S2(c): compositional analysis of the films was done by Rutherford Backscattering Spectrometry (RBS) that shows the expected 1:1 stoichiometry of Fe and Lu and a thickness that is in concordance with the results obtained by X-rays reflectometry. In Figure S2(d) we show an image of the surface obtained by atomic force microscopy (AFM) that indicates a very smooth surface.

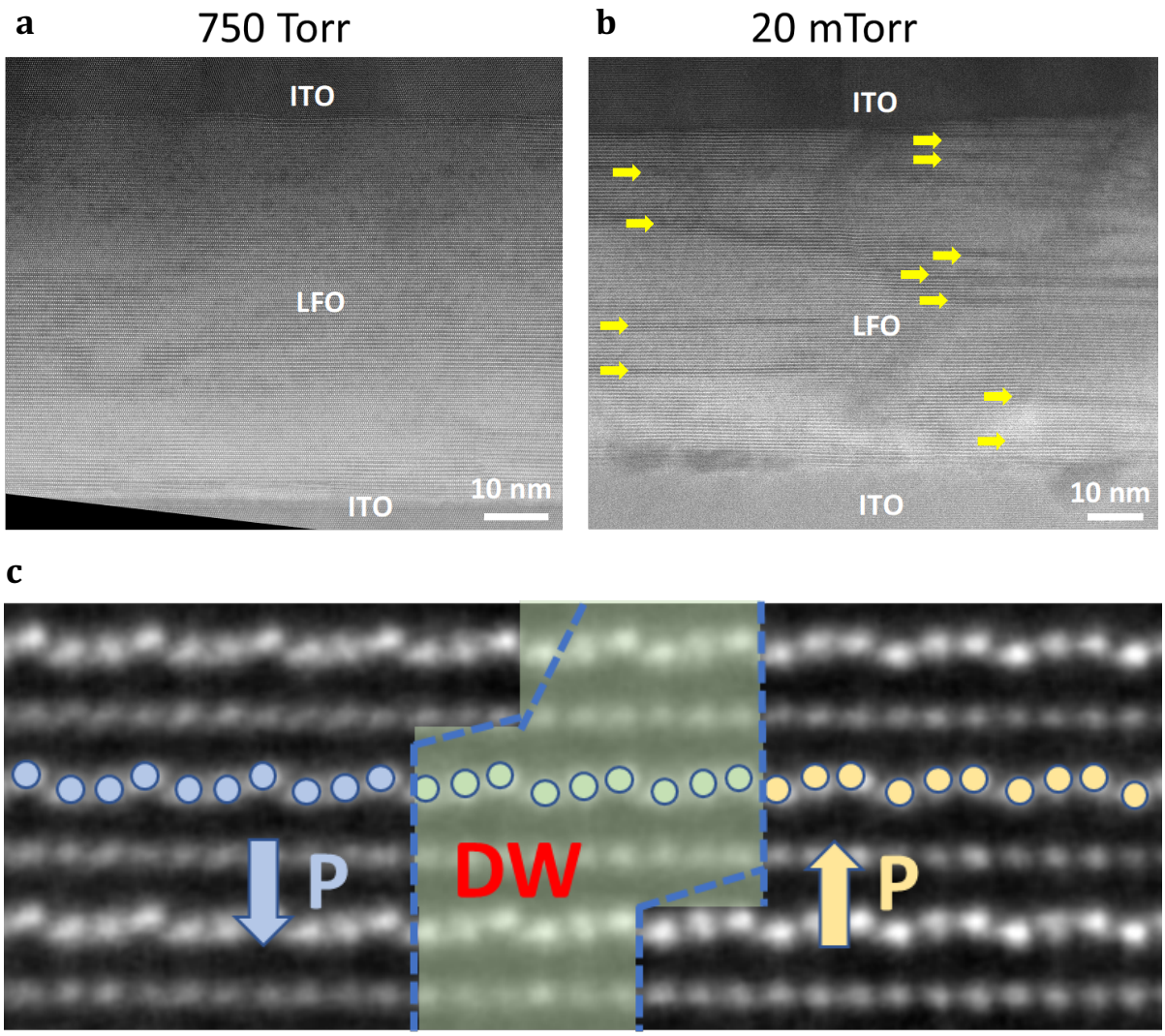

Supplementary Figure S3: **Microscopic changes in the structure induced by growth conditions.** The changes in the structure also can be observed in low magnification STEM images of the $LuFeO_3$ grown in different conditions. In Figure S3(a) we show image of the sample grown at the optimized condition with annealing in an oxygen pressure of 750 Torr; in this case we do not observe in the scale of image a large density of stacking defects, in contrast to the films annealed in lower oxygen pressures, (b). For the samples grown in the optimized condition but annealed at 20 mTorr (Figure S3 (b)) we observe a large density of stacking defects, identified by the yellow arrows. The presence of these defects is directly related to the reduction of the coercive voltage in the h-LFO. (c) Zoom-in on the region with 1-2-3 staircase.

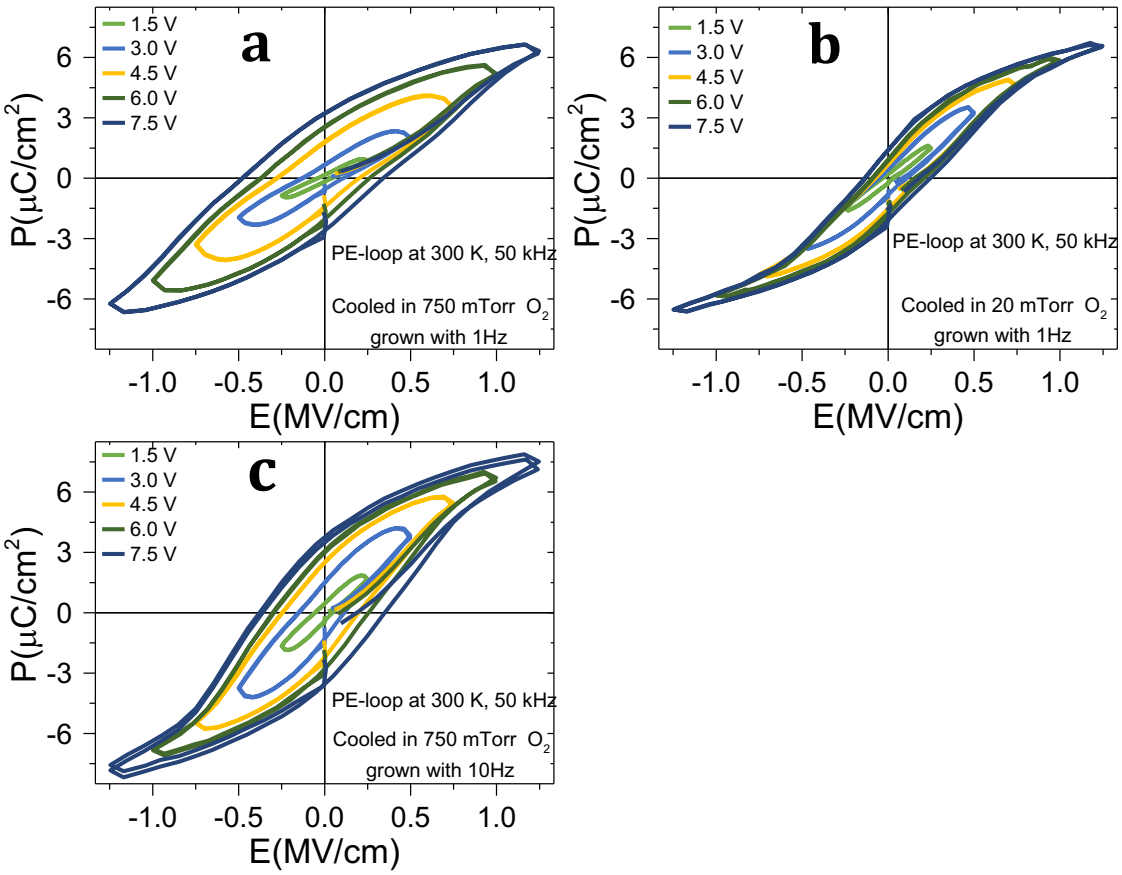

Supplementary Figure S4: (a-c) Ferroelectric hysteresis loops at 300 K of the Pt/ITO/LFO/ITO systems grown by PLD used in this study. (a) grown at a deposition rate of 1Hz, cooled in 750Torr of oxygen; (b) grown at 1 Hz and cooled in 20 mTorr of oxygen; (c) grown at 10Hz and cooled in 750 Torr of oxygen. The hexagonal $LuFeO_3$ shows robust ferroelectricity in all samples grown by PLD as shown in Figure S4 which shows good quality ferroelectric hysteresis at room temperature.

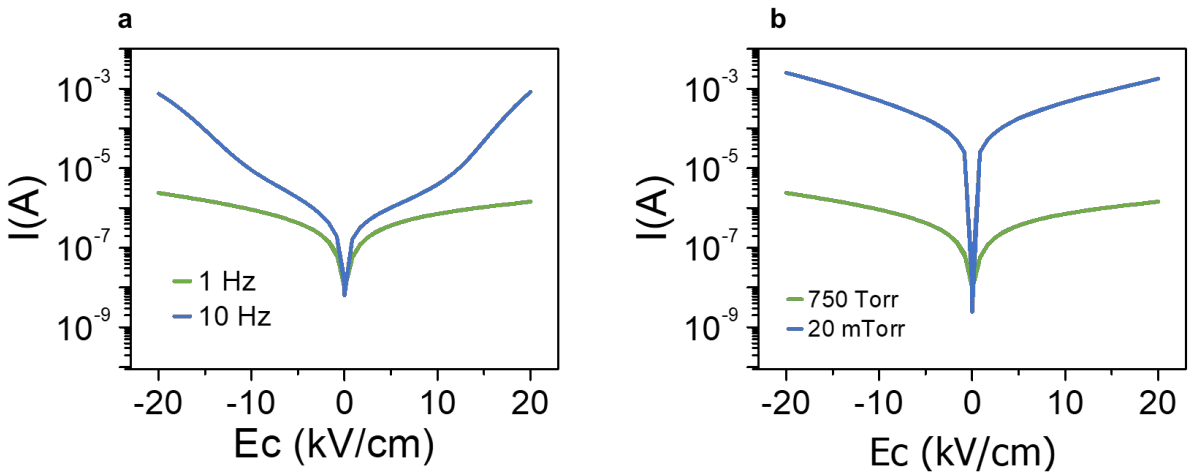

Supplementary Figure S5: A comparison of the current-voltage responses of (a) sample grown at a deposition rate of 1Hz, cooled in 750 Torr of oxygen (green line) with the sample grown at 10 Hz and cooled in 750 Torr of oxygen (blue line); (b) sample grown at a deposition rate of 1Hz, cooled in 750 Torr of oxygen (green line) with the sample grown at 1 Hz and cooled in 20 mTorr of oxygen; These results show that the more defective samples also show a larger leakage current at the macroscopic scale compared to the films that are of lower defect density.

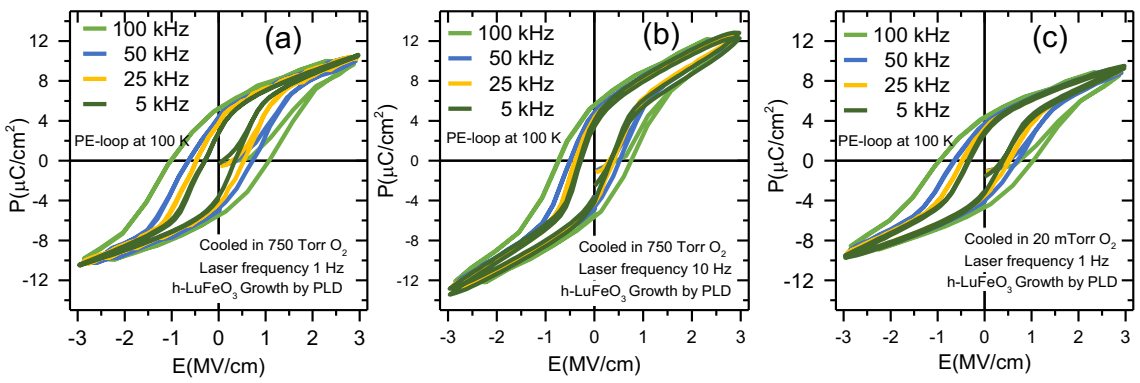

Supplementary Figure S6(a-c) Ferroelectric hysteresis loops of the three model systems used in this study as a function of test frequency at 100 K.

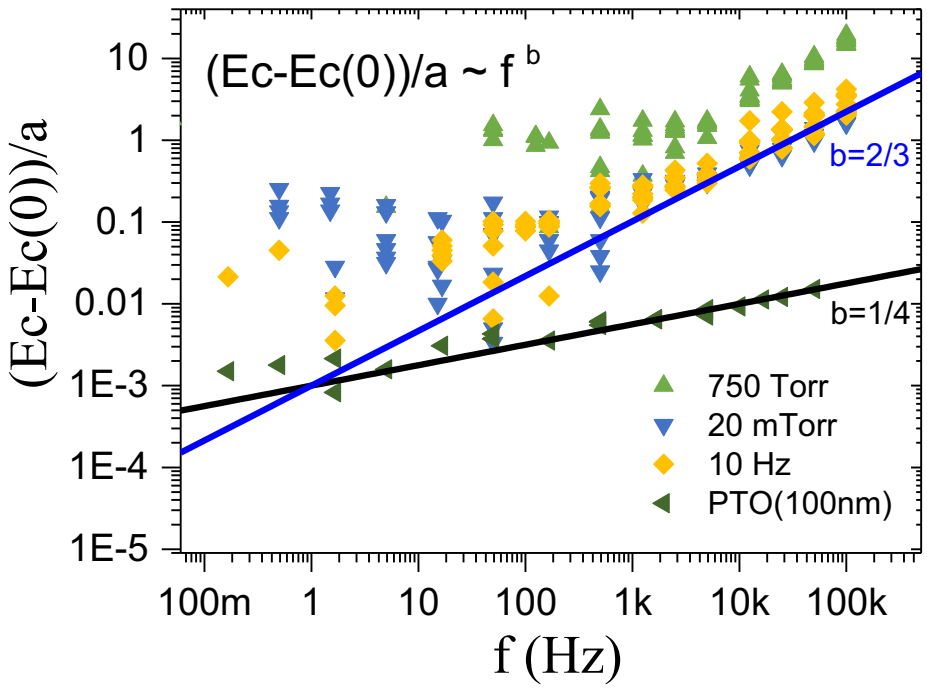

Supplementary Figure S7: A log-log "universal" plot of normalized switching field, i.e., $[Ec-E_c^0/a]$ as a function of frequency. The proper ferroelectrics (PTO and BFO) map onto each other with a slope of ~1/4. In contrast, the improper ferroelectric samples all show a two-stage frequency dispersion. Above ~100Hz, they all map approximately onto the same plot with a slope of 2/3.